

Superconductivity in CH_4 and BH_4^- Containing Compounds Derived from the High-Pressure Superhydrides

Nisha Geng^{a,1}, Katerina P. Hilleke^{a,1}, Francesco Belli^a, Pratik Kumar Das^a, Eva Zurek^{a,*}

^a*Department of Chemistry, State University of New York at Buffalo, Buffalo, 14226-3000, NY, USA*

Abstract

Inspired by the synthesis of the high-pressure $Fm\bar{3}m$ LaH_{10} superconducting superhydride, systematic density functional theory (DFT) calculations are performed to study ternaries that could be derived from it by replacing two of the hydrogen atoms with boron or carbon and varying the identity of the electropositive element. Though many of the resulting alkali-metal and alkaline-earth MC_2H_8 phases are predicted to be dynamically stable at mild pressures, their superconducting critical temperatures (T_c s) are low because their metallicity results from the filling of an electronegative band. Substitution with a trivalent element leads to phases with substantial metal d -character at the Fermi level whose T_c s are typically above 40 K. Among the MB_2H_8 phases examined, KB_2H_8 , RbB_2H_8 and CsB_2H_8 are predicted to be dynamically stable at very mild pressures, and their stability is rationalized by a DFT-Chemical Pressure analysis that elucidates the role of the M atom size. Quantum anharmonic effects strongly affect the properties of KB_2H_8 , the highest predicted T_c compound, near 10 GPa, but molecular dynamics simulations reveal it would decompose below its T_c at this pressure. Nonetheless, at ca. 50 GPa KB_2H_8 is predicted to be thermally stable with a superconducting figure of merit surpassing that of the recently synthesized LaBeH_8 .

Keywords: High-pressure, Crystal structure prediction, First-principles

*Corresponding author

Email address: ezurek@buffalo.edu (Eva Zurek)

¹These authors contributed equally

calculations, Hydrides, Superconductors, Electron-phonon coupling

1. Introduction

The search for hydrogen-rich materials with high superconducting critical temperatures (T_c s) has made great strides [1] in the two decades since Neil Ashcroft predicted that doping hydrogen with a second element could expedite its metallization thereby inducing superconductivity [2]. Ashcroft argued that the internal pressure applied by the doping atoms would “chemically precompress” the main hydrogen matrix, and lower the physical pressure required for metallization. Since then, a number of chemically intriguing and unexpected hydride phases with high T_c s have been successfully synthesized at pressures attainable in diamond anvil cells including H_3S ($T_c = 203$ K at 150 GPa [3]), LaH_{10} ($T_c = 260$ K at 200 GPa [4, 5]), YH_6 ($T_c = 220$ K at 183 GPa [6], or 224 K at 166 GPa [7]), CaH_6 ($T_c = 215$ K at 172 GPa [8], or 210 K at 160 GPa [9]), $(\text{La}, \text{Y})\text{H}_6$, ($T_c = 237$ K at 183 GPa [10]), and YH_9 ($T_c = 262$ K at 182 GPa [6]). However, challenges still remain: while these materials exhibit impressive T_c s, all require substantial pressure to prevent their decomposition. In fact, the discovery of these superconducting hydrides has spawned a new quest, this time for hydrogen-based high- T_c phases that remain stable at or near atmospheric pressures [11].

The pursuit of high- T_c superconductors has been greatly aided by the increasing speed and power of first-principles calculations. Since high-pressure experiments are expensive and difficult, much cheaper computations can screen candidate systems and identify promising leads. Crystal structure prediction (CSP) techniques [12, 13] have been key in this aspect. In fact, several of the previously mentioned high- T_c materials were first uncovered via CSP studies [14, 15, 16] prior to their experimental realization. These are the “clathrate-like” superhydrides, including those with MH_6 , MH_9 , and MH_{10} stoichiometries in which weakly covalently-bonded hydrogen atoms form three-dimensional networks that are able to encapsulate metal atoms. In contrast, $\text{Im}\bar{3}m$ H_3S belongs to another family of hydride superconductors built with covalent bonds between hydrogen and a main group non-metal [3, 17]. The binary M -H phase diagrams have been fairly exhaustively explored, with plenty of promise but still, no room-temperature ambient-pressure superconductors have been discovered [18]. Therefore, researchers have begun searching for superconductivity in ternary and even quaternary hydride phases.

A major obstacle, however, is the vast number of combinatorial possibilities that render Density Functional Theory (DFT) based CSP searches on a broad range of chemical combinations unfeasible. One way to lower the tremendous

computational cost is via the generation of machine-learned interatomic potentials that can roughly scan the phase space for promising compositions [19, 20, 21], which are later more thoroughly explored using DFT. In many cases, however, more traditional methods have come to the fore in the prediction of novel hydrides. One approach is to combine two already known superconducting binaries. For instance, a study that identified a $P\bar{6}m2$ CaSH_3 phase with a computed T_c of ~ 100 K at 128 GPa [22] was inspired by the prediction and synthesis of CaH_6 [14, 8, 9] and H_3S [3, 17]. A second approach is to add other elements into previously identified superconducting compounds, exemplified by substitutional doping in H_3S -based materials [23, 24]. Finally, DFT-based high-throughput searches on prototype structures that have been discovered either via CSP [25], or by ternary modifications of the binary superhydrides [26] have identified promising candidates that present a balance between high- T_c and low stabilization pressure. For example, theoretical predictions have suggested that two main modifications of $Fm\bar{3}m$ MH_{10} (Figure 1a) – the structure assumed by the first clathrate superhydride to be synthesized, LaH_{10} – result in ternary hydrides that can be quenched to lower pressures than the binary. The hydrogenic lattice in this structure can be viewed as a network of vertex-sharing H_4 tetrahedra and H_8 cubes. One pathway, by removing a hydrogen atom from the $8c$ Wyckoff site that lies in the center of the tetrahedra, and stuffing the H_8 cubes with Be or a p -block element results in phases with MXH_8 compositions [27, 26, 28, 29], exemplified by LaBeH_8 , which was synthesized and measured to have a T_c up to 110 K at 80 GPa [30].

The focus of the present investigation is a different modification of $Fm\bar{3}m$ MH_{10} , attained by replacing the hydrogen atoms at the $8c$ site with X (here, B or C) yielding the MX_2H_8 structure (Figure 1b). The pressure-dependence of the dynamic stability and superconducting properties of a few MX_2H_8 compounds has already been explored computationally including MC_2H_8 [31, 32, 33], MB_2H_8 [34, 35], and MN_2H_8 [36]. These initial studies suggest this family of compounds may present a viable route towards warm and light superconductivity manifested by KB_2H_8 , which has been predicted to maintain dynamical stability as low as 12 GPa ($T_c = 146$ K) [35], LaC_2H_8 with $T_c = 69$ K at 70 GPa [33], and YC_2H_8 with $T_c = 61$ K at 50 GPa [32]. The latter of these compounds was constructed on the basis of DFT-Chemical Pressure arguments, which interrogate the internal stresses within a crystal structure that arise due to atomic size. Unfortunately, since T_c estimates can be extremely sensitive to the methodology and the computational settings used, it is difficult to uncover trends in the aforementioned

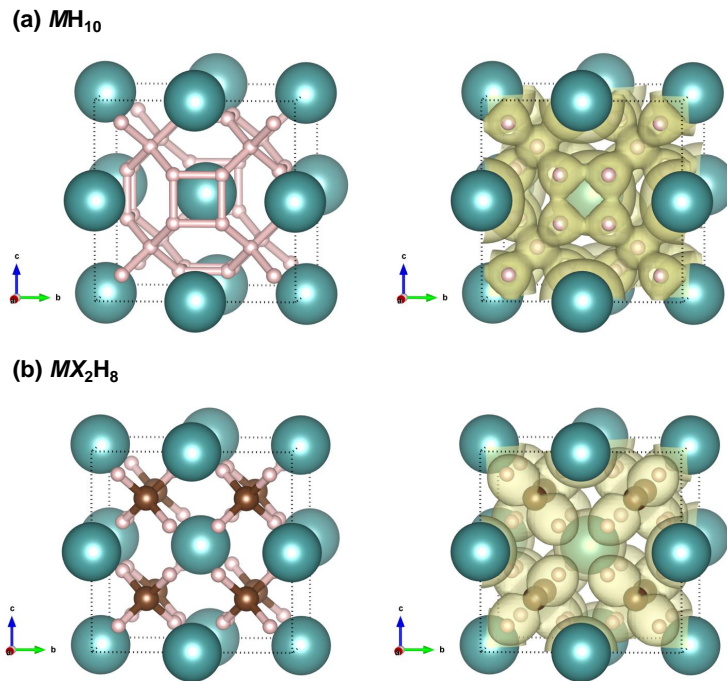


Figure 1: Illustrations of structure (left) and electron localization function plot (right) of the conventional cell of: (a) $Fm\bar{3}m$ MH_{10} and (b) $Fm\bar{3}m$ MX_2H_8 , where M is an electropositive metal atom and X denotes carbon or boron. $M/H/X$ atoms are colored green/pink/brown. Isosurface = 0.5 computed for $Fm\bar{3}m$ LaH_{10} and $Fm\bar{3}m$ KB_2H_8 at 300 GPa.

studies, which typically looked at no more than a few compositions.

Therefore, herein we performed systematic high-throughput calculations on $Fm\bar{3}m MX_2H_8$ compounds varying the identity of the electropositive metal atom ($M = \text{Li, Na, K, Rb, Cs, Be, Mg, Ca, Sr, Ba, Sc, Y, and La}$) for both B and C substitutions. Their dynamic stability, electronic structure and propensity for superconductivity was computed, as a function of pressure from ambient to 300 GPa. Such studies can uncover a plethora of chemical trends, for example the connection between stability and ionic radii of the electropositive element, and oxidation state of the metal atom with the predicted T_c , facilitating the comparison of the properties of a single structure with different elemental compositions [37]. We find that from the 26 different MB_2H_8 and MC_2H_8 compounds considered, 14 are (phonon) metastable at various points from ambient to 300 GPa, some to as low as 4 GPa. Though a number of the MC_2H_8 species were metallic and stable, only those containing a trivalent metal element had appreciable T_c s below ~ 200 K. In addition, we considered the effects of atomic size on dynamical stability and the role of valence electron count on T_c , finding that univalent M atoms yield both a strong electron phonon coupling and high T_c even at low pressures within MB_2H_8 compounds. Moreover, quantum nuclear effects were found to renormalize the frequencies of the phonon modes and resulting electron-phonon coupling strength within KB_2H_8 , the phase with the highest predicted T_c at the lowest pressure, which was predicted to thermally decompose below its T_c at 12 GPa. Molecular dynamic simulations suggest that at least 50 GPa is required to stabilize KB_2H_8 to temperatures surpassing its isotropic Eliashberg T_c , 85 K.

2. Computational Details

Geometry optimizations, molecular dynamics simulations, and electronic structure calculations including band structures, densities of states (DOS), electron localization functions (ELF), and Bader charges were calculated by density functional theory (DFT) as implemented in the Vienna *ab-initio* Simulation Package (VASP) version 5.4.1 [38, 39]. The gradient-corrected exchange and correlation functional of Perdew-Burke-Ernzerhof (PBE) [40] was employed along with the projector augmented wave (PAW) method [41]. The plane-wave basis set energy cutoff was 900 eV and the B $2s^22p^1$, C $2s^22p^2$, and H $1s^1$ electrons were treated explicitly in all of the calculations. The valence configurations and PAWs employed for the metal atoms are listed in Table S1. The Γ -centered Monkhorst-Pack scheme was used to produce k -point meshes chosen so that the product of

the number of divisions along each reciprocal lattice vector with the real lattice constant was 50 Å in the geometry optimizations, and 70 Å otherwise. The crystal orbital Hamilton population (COHP) and the negative of the COHP integrated to the Fermi level (-iCOHP), calculated by the LOBSTER package [42], were used to estimate the bond strengths within selected phases. The optimized structural parameters are provided in Table S17-S18. The thermal stability of KB_2H_8 at 3, 12, and 50 GPa (and YC_2H_8 at 50 GPa) was examined by performing *ab initio* molecular dynamics (AIMD) simulations using a canonical NVT ensemble at 77, 165, and 300 K, with temperature and volume controlled via a Nosé-Hoover thermostat [43, 44, 45, 46]. A $2 \times 2 \times 2$ supercell was chosen to reduce the constraint of periodic boundary conditions with an energy cutoff of 600 eV, and only the Γ -point was used. All AIMD simulations contained 10,000 MD steps (10 ps). High-throughput phonon calculations were carried out using the VASP package coupled with the PHONOPY code [47].

The electron-phonon coupling (EPC) calculations were performed with the Quantum Espresso (QE) program package [48]. The B $2s^22p^1$, C $2s^22p^2$, H $1s^1$ and metal pseudopotentials (Table S1) were obtained from the PSLibrary [49], and generated by the method of Trouiller-Martins [50]. The plane-wave basis set energy cutoffs varied from 80-120 Ry (Table S2). The Brillouin zone sampling scheme of Methfessel-Paxton [51] was applied with a smearing width of 0.01-0.03 Ry (Table S2). A $16 \times 16 \times 16$ k -point grid was used for all phonon calculations, while a dense $32 \times 32 \times 32$ k -point grid and an $8 \times 8 \times 8$ q -mesh was used for all of the EPC calculations. The EPC parameter, λ , was calculated using a set of Gaussian broadenings from 0.0 to 0.500 Ry (with an increment of 0.005 Ry) and converged to 0.05 Ry. The T_c s were estimated using the Allen-Dynes modified McMillan equation [52] with a renormalized Coulomb potential, μ^* , of 0.1. For those systems with an EPC constant, λ , larger than unity the T_c s were calculated via numerical solution of the Eliashberg equations [53]. The quantum nuclear effects and anharmonicity on the dynamical stability and superconducting properties of $Fm\bar{3}m$ KB_2H_8 were studied using the Stochastic Self Consistent Harmonic Approximation (SSCHA) [54]. The quantum anharmonic phonon spectra was calculated at 0 K, in a $2 \times 2 \times 2$ supercell, using up to 3000 configurations containing 88 atoms each, and including terms up to the fourth order in the calculation of the free energy Hessian. The self consistent calculations required for the stochastic sampling were performed using the QE program package with parameters commensurate to those specified above.

A DFT-Chemical Pressure Analysis [55], which visualizes the internal stresses

inherent in a crystal structure as a consequence of steric constraints, was performed on select phases using the *Cpackage2* [56] coupled with output from relevant modules [57, 58], as described fully in Section S1.3. The compounds examined: LiB_2H_8 , NaB_2H_8 , KB_2H_8 , RbB_2H_8 , and CsB_2H_8 , were optimized at 0 GPa using the ABINIT [59] software package and LDA-DFT (Section S8).

3. Results and Discussion

Our high-throughput DFT calculations showed that fourteen out of the twenty-six chemical compositions studied were dynamically stable, having no imaginary phonon frequencies throughout the whole Brillouin Zone, within an element-dependent pressure range. From these, seven – NaC_2H_8 (6 GPa), KC_2H_8 (4 GPa), RbC_2H_8 (15 GPa), MgC_2H_8 (10 GPa), KB_2H_8 (12 GPa), RbB_2H_8 (16.5 GPa) and CsB_2H_8 (20 GPa) – were dynamically stable at the near-ambient pressures that are given in the braces. The remaining seven – CsC_2H_8 , CaC_2H_8 , SrC_2H_8 , ScC_2H_8 , YC_2H_8 , LaC_2H_8 , and BaB_2H_8 – required at least 50 GPa to prevent their vibrations from inducing structural phase transitions. These results are plotted graphically in Figure 2, where the dynamically stable phases are denoted by rectangles color-coded according to their predicted T_c from blue (cold) to red (hot). Insulating compounds are denoted by a dark blue rectangle, and those that are dynamically unstable are left empty.

Some of these systems have been studied computationally before. Yttrium [32] and lanthanum-containing [33] $Fm\bar{3}m$ MC_2H_8 phases were predicted to remain dynamically stable to pressures as low as 50 GPa and 70 GPa, respectively. Jiang *et al.* uncovered several more MC_2H_8 phases containing Na (20-100 GPa), K (50-100 GPa), Mg (20-40 GPa), Al (10-100 GPa), and Ga (20-100 GPa) to be dynamically stable in the pressure ranges provided in the braces [31]. Turning to the boron containing compounds, Gao *et al.* and Durajski *et al.* found $Fm\bar{3}m$ KB_2H_8 to be dynamically stable from 12-200 GPa [35] and 3-100 GPa [60]. A later CSP study by Li *et al.* identified this to be the most stable KB_2H_8 phase between 30-100 GPa, but at lower pressures an $I4_1/a$ symmetry structure was preferred instead [34]. CSP was also employed to search for the most stable MB_2H_8 phases across the range of alkali metal atoms (excluding francium) and only KB_2H_8 , RbB_2H_8 and CsB_2H_8 were computed to be dynamically stable above 10 GPa [34]. In a related work, the pressure dependant dynamic stability of ammonium containing systems with the general formula MN_2H_8 and a variety of metal atoms was computationally investigated [36]. As described below, our study uncovered six dynamically

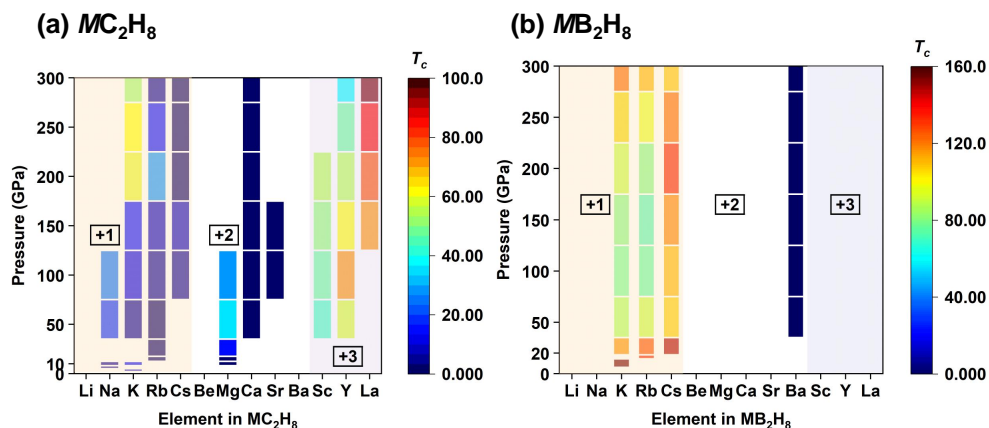


Figure 2: A map of the superconducting critical temperature, T_c , calculated via numerical solution of the Eliashberg equations and assuming a Coulomb repulsion parameter, $\mu^* = 0.1$, of (a) MC_2H_8 and (b) MB_2H_8 from 0 GPa to 300 GPa with 50 GPa increments. The identities of the metal atoms are given on the x -axes, with the various regions color coded by the metal valence (+1, +2, or +3). For the lower pressures the T_c map is colored by values obtained in the middle of the pressure interval, while for pressures above 50 GPa the T_c was calculated at the end of the pressure interval (Table S9-S11).

stable species that were not predicted in these previous investigations: RbC_2H_8 , CsC_2H_8 , CaC_2H_8 , SrC_2H_8 , ScC_2H_8 and BaB_2H_8 , and extended the pressure range probed for dynamical stability from 4 GPa to 300 GPa. Let us now examine the electronic structure and propensity for superconductivity in these compounds.

In contrast to their cousin MH_{10} and MXH_8 structures (e.g. LaH_{10} and $LaBH_8$), for which the hydrogen atoms adopt a loose covalent 3-D network, the MX_2H_8 phases examined herein present a rather different bonding environment. The placement of the B or C atoms in the metal hydrogen framework renders them tetrahedrally coordinated by hydrogen atoms, leading to the formation of molecular BH_4^- or CH_4 units. Whereas the ELF isosurface encapsulates the 3-D hydrogenic framework in MH_{10} , for MX_2H_8 high values of the ELF, suggestive of covalent bonding, are present along the B-H and C-H contacts, but the ELF between hydrogen atoms in neighboring BH_4^- or CH_4 fragments is very low (e.g. see Figure 1). For example, for KB_2H_8 , the ELF reaches a minimum value of 0.14 at the midpoint between these hydrogen atoms (separated by 1.90 Å at 12 GPa). Increasing the pressure to 300 GPa pushes the BH_4^- units closer together so that

the shortest distance between their hydrogens measures 1.20 Å, but the ELF at the midpoint increases only slightly to 0.37. In both cases, there is a sharp delineation between the ELF isosurfaces associated with different BH_4^- subunits. For comparison, in $Fm\bar{3}m$ LaH_{10} at 150 GPa, the ELF value reaches a minimum of 0.64 between the $8c$ and $32f$ H atoms and 0.52 for the contacts between $32f$ H atoms (analogous to the inter- BH_4^- H-H contacts in KB_2H_8).

How might we understand the curious trends seen in Figure 2, as to which metal atoms result in dynamically stable MX_2H_8 phases? One difficulty arises from the fact that the MB_2H_8 and MC_2H_8 systems appear to require different metal atoms to be phonon-stable (at some pressure in the range considered): for MC_2H_8 this includes the alkaline earths (except Be and Ba) as well as trivalent Sc, Y, and La. In MB_2H_8 phases, on the other hand, dynamical stability is only achieved with barium (from the alkaline earths) and none of the trivalent phases correspond to local minima. The only commonality is in a subset of the alkali metals: K, Rb, and Cs. Thus, for both MB_2H_8 and MC_2H_8 systems, the larger alkali metals confer dynamical stability, with NaC_2H_8 also being dynamically stable but not NaB_2H_8 . This trend could be elucidated through the DFT-Chemical Pressure method [55, 56], which, based on the quantum mechanical stress density, interrogates the interatomic tensions within a crystal structure that come from atomic packing. Analyzing these tensions reveals regions where shrinking or expanding the unit cell would be energetically favorable. A particular crystal structure with DFT-relaxed coordinates represents a balance of these tensions. Here, we will investigate the role played by the alkali metals Li, Na, K, Rb, and Cs in the dynamical stability – or lack thereof – of the MB_2H_8 compounds, because a subset of them are predicted to have high T_c s at relatively low pressures (Figure 2).

In a DFT-Chemical Pressure scheme, the internal conflicts of atomic size in a particular crystal structure are displayed as “chemical pressures”, whose resolution can drive structural distortions or phase transitions [61, 32, 62]. Here, the CP schemes in question are shown in Figure 3. In these images, each atom is surrounded by a black-and-white surface whose shape is derived from spherical harmonic functions, with the M (= Li, Na, K, or Rb) and B atoms further surrounded by orange and green translucent spheres for visual clarity. The distance from the atom to the spherical-harmonic-like surface represents the magnitude of CP in that direction, with the character being represented by the color of the surface: black for negative CP, where interatomic distances are too long and shrinking of the local coordination would be favorable, and white for positive CP, where the coordination environment is overly cramped and interatomic distances are too

short.

Overall, the DFT-CP schemes calculated for the four MB_2H_8 phases are qualitatively similar. The alkali metal atoms display positive, but small, CP lobes along the three Cartesian axes, with those for Li being particularly tiny due to the poor fit of the small cation between the BH_4^- units. These positive CPs, directed towards the nearby H atoms from surrounding BH_4^- units, are echoed in the most prominent positive CP lobes on the H atoms directed right back at the M atoms (Figure 3b). Negative CPs fill in the rest of the space around the metal atoms, loosely directed towards the B atoms. The CP features decorating the B atoms, which are mainly due to the close B-H interactions, are fairly consistent in magnitude across the MB_2H_8 series, with slight negative CP directed towards the M atoms and stronger positive CP towards the H. On the H atoms, negative CPs are directed towards the H atoms in neighboring BH_4^- units, while between the B and H atoms are positive CPs.

The consistency of the B-H CP features across the structural series indicates a generally rigid BH_4^- subunit – in this case, one held in place by strong covalent bonds. How well the M atom fits into the interstices of the BH_4^- sublattice should then govern the dynamical stability. For each member of the structural series shown, the net CP on the M atoms is negative, indicating a coordination environment that is roomy rather than constrained. However, the magnitude of the CP features decorating the M atoms decreases as their size increases, with the CP lobes on the K and Rb atoms being much reduced in comparison to Li and Na. This reflects an improved fit of the alkali metal atom to the interstices of the BH_4^- network, borne out in a dynamically stable structure.

In fact, the DFT-CP schemes of the MB_2H_8 phases can provide additional information about the lattice dynamics (to be interrogated in detail below). Negative and positive CPs, especially when perpendicular to one another, are correlated with soft and hard phonon modes, respectively. High frequency modes in the MB_2H_8 phases examined here correspond to B-H stretches, which we expect from the CP picture to be high in energy due to the positive CP between B and H atoms. Furthermore, as discussed below, the EPC in KB_2H_8 has strong contributions from twisting motions of the H atoms in the BH_4^- units. Such low-frequency motions lie along the directions of negative H-H CP – and for LiB_2H_8 and NaB_2H_8 , dip into the imaginary regime. Perhaps, here, the smaller Li and Na atoms are not able to prevent, via steric intervention, the motions of the BH_4^- clusters from driving the structure into dynamical instability.

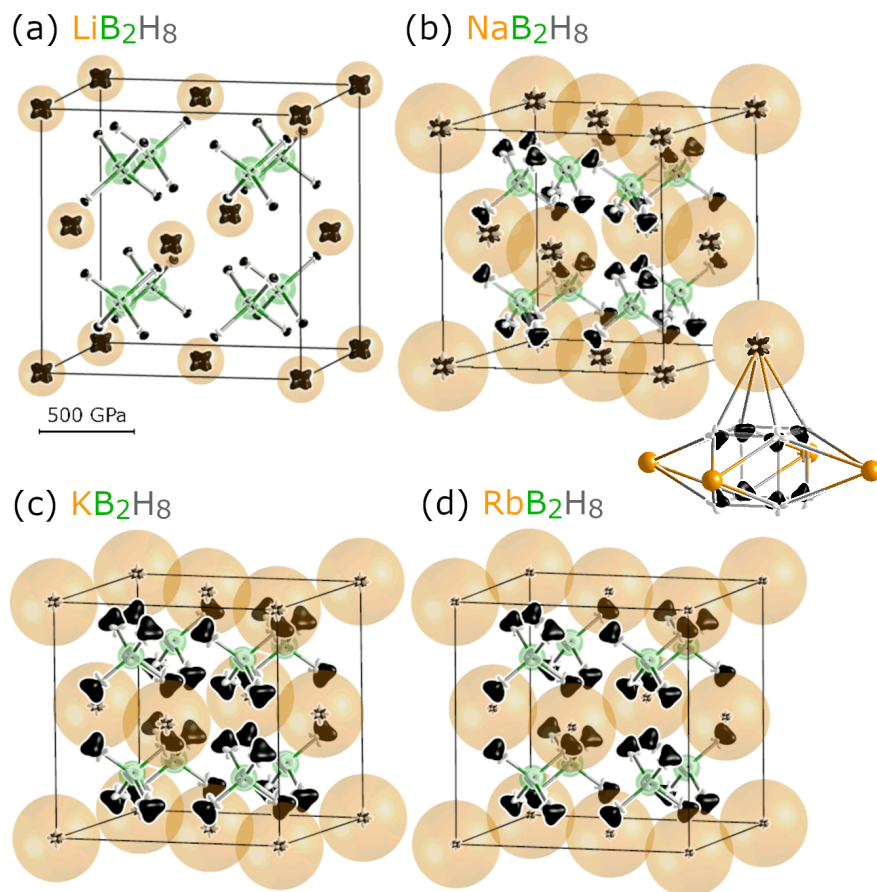


Figure 3: DFT-Chemical Pressure schemes calculated for (a) LiB_2H_8 , (b) NaB_2H_8 , (c) KB_2H_8 and (d) RbB_2H_8 at 0 GPa. Chemical pressures surrounding each atom are projected onto spherical harmonic functions, with black lobes corresponding to negative (favoring contraction) and white lobes to positive (favoring expansion) chemical pressures. A scalebar is included for comparison; all CP schemes have been plotted to the same scale. M and B atoms are highlighted with orange and green translucent spheres. As the size of the M atom increases, the magnitude of the CP features decreases, while the features on the B and H atoms are relatively consistent. Positive CP occurs between the B and H atoms as well as between the M and H atoms (inset to (b) shown to highlight the M - H interaction), with negative CP mostly within the H lattice as well as along M - B contacts.

How do the various intercalating elements affect the electronic properties of these phases? The number of electrons that can participate in the superconducting mechanism is linked to the density of states (DOS) at the Fermi level (E_F), which is therefore a key descriptor in predicting the T_c of conventional superconductors [63]. The PBE-computed DOS at E_F ($g(E_F)$) at various pressures was obtained and is tabulated in Table S7-S8. for the studied MB_2H_8 and MC_2H_8 phases. Compounds containing CH_4 or BH_4^- molecular units are typically non-metallic, but combining them with electropositive elements of the appropriate valence may result in the formation of metallic systems, whose molecular vibrations are involved in superconductivity. This strategy has been explored previously via computations on $Ba_x(CH_4)_{1-x}$ ($T_c = 44$ K at 90 GPa) [64], $BeCH_4$ ($T_c = 30$ K at 80 GPa [65]), and $MgCH_4$ ($T_c = 120$ K at 105 GPa) [66]. Hole doping insulating $Ca(BH_4)_2$ with K has been predicted to yield T_c s as high as 110 K at ambient pressures [67], and various molecular or extended B-H motifs metallized by electron donation from an electropositive element have been explored in the computational search for superconductivity in compounds with covalent bonds driven metallic via charge reorganization [68, 69, 70, 71].

CH_4 is a neutral molecule, methane. When combined with a metal intercalant, as in the MC_2H_8 phases, charge is transferred from the electropositive metal atoms to methane-based anti-bonding bands, rendering CH_4 slightly anionic. Nevertheless, the $CH_4^{\delta-}$ units are predicted to be dynamically stable even to high pressures (ca. 300 GPa) in some of the studied compounds (Figure 2). To highlight some of the noted trends, band structures and DOS plots of select structures are provided in Figure 4. In KC_2H_8 E_F lies at the top of a peak in a feature of the DOS that corresponds to a half-filled band, resembling the electronic structure of $Fm\bar{3}m$ Mg_2IrH_6 , which was predicted to have a T_c of 160-175 K at ambient pressure [21]. Full charge transfer from the potassium would result in an excess of 0.5 electrons on each methane molecule, suggesting the presence of a quarter filled doubly degenerate band crossing E_F . The band structure we calculate, however, is markedly different. To better understand the origin of the metallicity of this phase, we note that the lowest unoccupied molecular orbital (LUMO) of methane, of $3a_1$ symmetry, is mainly derived from an out-of-phase combination of the carbon and hydrogen s -orbitals. This orbital is very diffuse, Rydberg-like, with a node near the hydrogen atoms, stemming from the contribution of higher lying orbitals.

The LUMO of ammonia has a qualitatively similar appearance. A detailed quantum mechanical study on $(NH_3)_n^{\delta-}$ clusters showed that the overlap of the

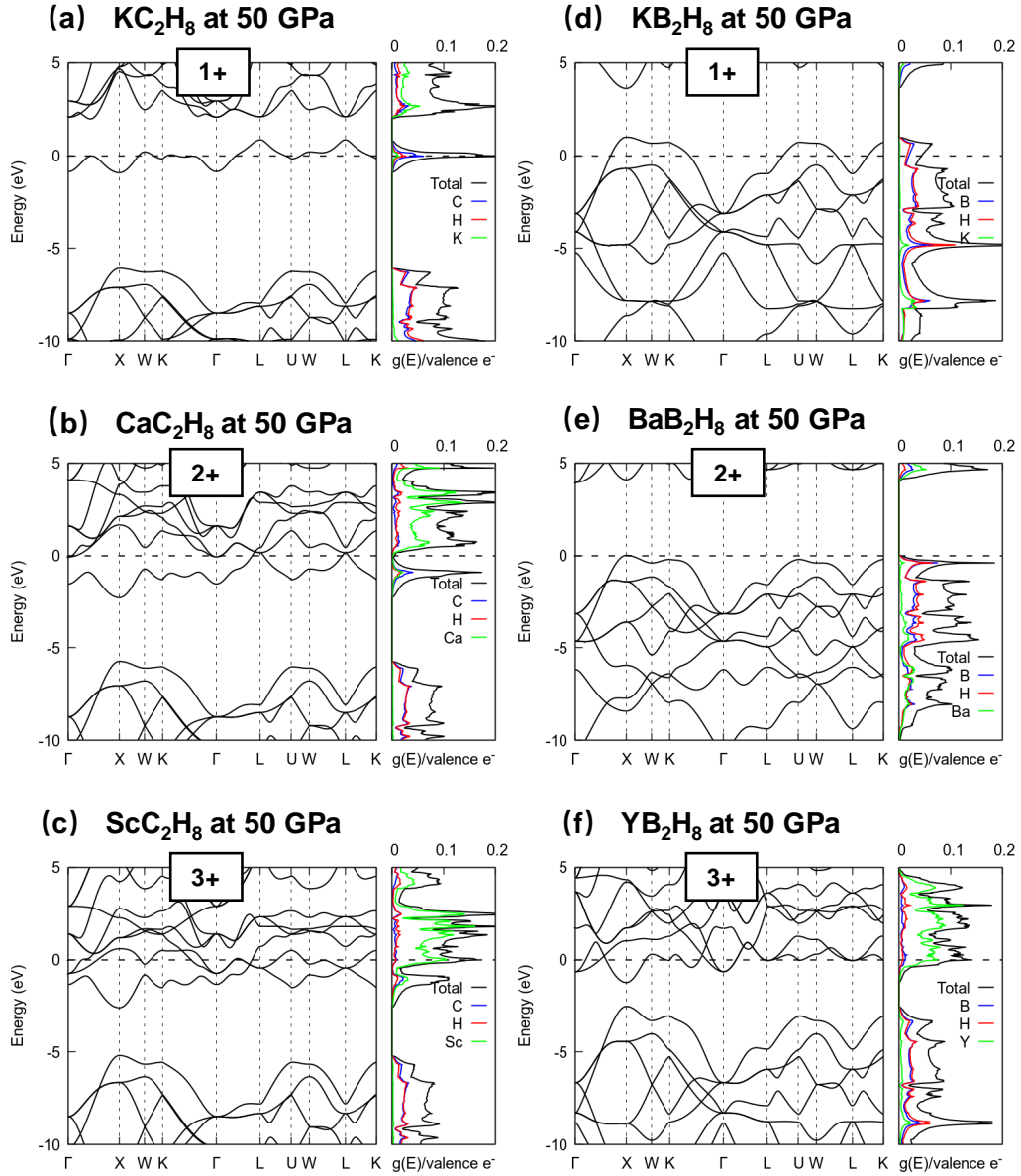


Figure 4: Representative electronic band structures and projected densities of states at 50 GPa for MX_2H_8 phases that contain electropositive metals, M , with varying formal oxidation states: (a) KC_2H_8 (+1), (b) CaC_2H_8 (+2), (c) ScC_2H_8 (+3), (d) KB_2H_8 (+1), (e) BaB_2H_8 (+2), and (f) YB_2H_8 (+3). The top of the valence band (e) or Fermi energy (elsewhere) is set to 0 eV.

partially occupied LUMOs of the ammonia molecules results in a new type of bonding, denoted as $H \leftrightarrow H$ bonding [72]. In fact, such $H \leftrightarrow H$ bonding, this time stemming from the overlap of the $\text{Li}(\text{NH}_3)_4$ singly occupied molecular orbitals (SOMOs) in lithium(0)tetraamine solid, which also possess the same Rydberg-like characteristics, leads to a build up of charge in the interstices between molecules rendering this system an electride [73]. It turns out that the peculiar electronic structure of KC_2H_8 can be explained by this same mechanism. Within it the 4b Wyckoff position is surrounded by eight hydrogen atoms from nearby methane molecules. As charge is transferred to the CH_4 units their diffuse LUMOs overlap forming weak, but numerous $H \leftrightarrow H$ interactions, leading to a build-up of charge between them. Indeed, an isosurface and contour plot of the charge density associated with the filled portion of the metallic band illustrates that it corresponds to an interstitial blob, characteristic of an electride phase (Figure 5). There is one such blob per formula unit, corresponding to a single band, which is half-filled via transfer from the electropositive K atom. The H-to-blob-center distances measure 2.02 Å at 4 GPa, decreasing to 1.24 Å at 300 GPa. Curiously, the position of the blob also corresponds to the location of the beryllium atom in LaBeH_8 (and the *p*-block elements in related phases) – in line with expectations based upon chemical template theory [74]. CaC_2H_8 (Figure 4b) is a semi-metal resulting from the filling of this cavity-centered band. In ScC_2H_8 (Figure 4c) the Fermi level is shifted higher yet, and another set of bands crosses E_F , this time with substantial scandium *d*-character.

For a particular metal atom, the electronic structure of the MB_2H_8 compounds is markedly different from the analogous carbon-containing systems as BH_4^- is isoelectronic with CH_4 . Indeed, KC_2H_8 is a hole doped version of potassium borohydride – studied intensely for its potential as a hydrogen storage medium – with a sizeable $g(E_F)$, whereas BaB_2H_8 (Figure 4e) is an insulator. Previously experiments have identified several KBH_4 phases including those with cubic $Fm\bar{3}m$ (1 atm), tetragonal $P4_21c$ (4 GPa), and orthorhombic $Pnma$ (7 GPa) symmetry, which were reported to be semiconducting [75]. YB_2H_8 (Figure 4f) is isoelectronic with KC_2H_8 , and its half-filled band runs-up-and-down in the same manner as the metallic band within KC_2H_8 . However a key difference is that bands with Y-character, which is mostly *d*-like, hybridize with this blob-based band, and there is no gap between it and other higher lying bands. Moreover, neither YB_2H_8 nor any of the other trivalent elements considered were dynamically stable at any point in the whole pressure range studied.

Both the carbon and boron containing compounds exhibit a high $g(E_F)$ when

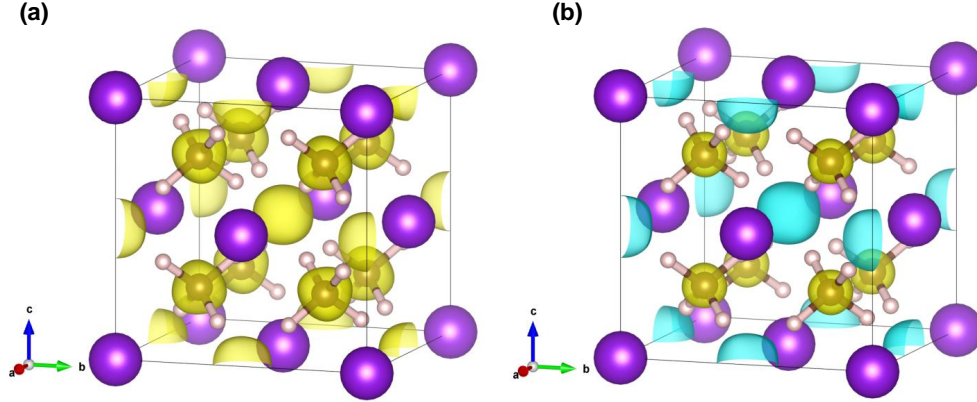


Figure 5: The charge density associated with the occupied part of the metallic band in KC_2H_8 at 50 GPa. (a) Isosurface with an isovalue of $0.005 e/\text{\AA}^3$. (b) Two-dimensional contour plot that cuts along the (1,0,1) plane colored from blue ($0.000016 e/\text{\AA}^3$) to red ($0.009 e/\text{\AA}^3$).

the metal atoms they contain are univalent or trivalent, making them potential superconductors. Compounds with bivalent elements, on the other hand, do not have an electronic structure conducive for superconductivity. For many of the methane-containing compounds increased pressure decreases $g(E_F)$ (Table S7-S8). One exception is KC_2H_8 where the Fermi level falls right below a peak in the DOS at low pressures. As pressure increases to 100 GPa, so does $g(E_F)$, and the Fermi level becomes coincident with the peak in the DOS. At higher pressures the DOS associated with the metallic band begins to bifurcate, as a pseudogap opens up, resulting in a decreased $g(E_F)$. For KB_2H_8 , RbB_2H_8 and CsB_2H_8 the DOS at E_F initially decreased, then plateaued, followed by an increase to 300 GPa (for $M = \text{K}, \text{Rb}$) or 200 GPa ($M = \text{Cs}$). The (PBE) bandgap of BaB_2H_8 decreased from 3.95 to 1.01 eV as pressure increased from 50-300 GPa.

The superconducting properties of the dynamically stable, metallic phases were calculated in 50 GPa intervals and the T_c s were estimated using the Allen-Dynes-modified McMillan (MAD) equation [52] and via numerical solution of the Eliashberg equations [53], which gives a more accurate result for systems with coupling constants, λ , larger than unity. Previous computations on YH_6 and YH_9 found almost isotropic superconducting gaps [76], and therefore we have not considered anisotropy in this work. The estimated Eliashberg T_c s are summarized in Figure 2, where dynamically stable phases are colored according to

their estimated T_c s. Tabulated Eliashberg and MAD T_c estimates are provided in Table S9-S11.

Though the MC_2H_8 compounds containing univalent metal atoms possessed a high $g(E_F)$, their predicted T_c s typically fell below 20 K. This can be understood by considering the nature of their metallic bands, associated with the interstitially localized electrons (as confirmed by visualizing the charge density associated with the filled portion of the metallic band, which were analogous to the one shown in Figure 5). Comparing to high pressure hydrides or cuprates, the T_c of electrides is typically quite low [77, 78], potentially because the vibrations of the blob-based-states are not expected to yield a high EPC. The only exception is KC_2H_8 where T_c is predicted to surpass 40 K above 200 GPa. For bivalent atoms, like CaC_2H_8 , E_F falls in a pseudogap, generally rendering them poor superconductors. The only exception to this trend is MgC_2H_8 , which is estimated to have a T_c of 19-35 K within its range of dynamic stability. The systems comprised of trivalent metal atoms are predicted to possess T_c s ranging from 40-100 K above 50 GPa, with a maximum T_c of 94.0 K computed for LaC_2H_8 at 300 GPa.

Our calculated T_c s for KB_2H_8 (155 K at 12 GPa), RbB_2H_8 (73 K at 50 GPa) and YC_2H_8 (58 K at 50 GPa) are comparable to previously reported values (146 K [35], 75 K [34], and 61 K [32], respectively, at the same pressures). The highest T_c s of 134-155 K, computed for the alkali- B_2H_8 phases, are observed for pressures below 20 GPa; at higher pressures T_c falls to as low as 70 K between 20-200 GPa and then increases again to as high as 121 K at 300 GPa within the Migdal-Eliashberg theory, and neglecting quantum lattice and anharmonic effects. For the reasons described above BaB_2H_8 was not predicted to be superconducting, and combinations with other metal atoms were not dynamically stable within the harmonic approximation.

Previous studies of alkaline- B_2H_8 phases [35, 34, 60] did not look into the vibrations related to the large computed EPC (Table S11). Herein, we examined the phonon vibrations that were key for the large λ of KB_2H_8 , as it has the highest predicted T_c at the lowest pressure. Figure 6 plots the phonon band structures, from low to high pressures, where red circles were utilized to represent the size of the contribution to the EPC constant at a particular wavevector \mathbf{q} and frequency ν . At 12 GPa, a strong EPC contribution is due to the soft mode at X resulting from a rocking motion of the BH_4^- units. This soft mode remains until the pressure increases to 50 GPa, where there is no single vibration that dominates the EPC. As pressure increases to 250-300 GPa, another soft mode appears in the phonon

spectrum at the L -point with a strong contribution to λ involving an asymmetric scissoring within the BH_4^- units, where one H atom bounces between two others to form short, transient, H-H contacts.

The soft phonon modes present in the band structure computed for KB_2H_8 at 12 GPa (Figure 6(a)) hint that quantum nuclear effects and the consequent anharmonicity could potentially be important in renormalizing the frequencies associated with the phonon modes and their corresponding EPC matrix elements [79]. Indeed, previous calculations on LaBH_8 , whose structure, like KB_2H_8 , can be derived from the parent metal MH_{10} superhydride, is quite susceptible to these effects [80]. Specifically, it was shown that solving the Schrödinger equation related to the Born-Oppenheimer energy surface with the addition of the ionic kinetic energy elongates the B-H distances with a concomitant softening of the phonon modes with hydrogen character. As a result, the phase was predicted to become dynamically unstable at a notably higher pressure than predicted by phonon calculations performed under the harmonic approximation. At the same time, these effects increased the EPC and therefore the computed T_c . Similar conclusions have been reached for H_3S [79] and LaH_{10} [81].

Therefore, quantum nuclear effects have been studied on the phonon band structure of KB_2H_8 at 5, 12 and 20 GPa (Figure S27). As compared to the harmonic phonons, the quantum nature of the nuclei introduces a separation between the various phonon branches with the upper branch undergoing a red shift, while the intermediate optical branch is squeezed into a smaller range of frequencies, in-line with what would be expected for strong anharmonic behavior. These variations are minimal at 20 GPa but become significant by 12 GPa. In the quantum case the instability near the X -point (Figure S27) is healed, and this phase is predicted to remain dynamically stable to a pressure slightly higher than 5 GPa where another instability, this time close to Γ , appears (as illustrated in the inset of Figure S27).

For classical nuclei, the electron-phonon coupling parameter, λ , logarithmic average of the phonon frequencies, ω_{\log} , and computed T_c are plotted for KB_2H_8 as a function of pressure in Figure 6(d) and its inset. Results obtained for quantum nuclei are also shown (see also Table S12). Comparing with the classical results, the value of λ is slightly increased at 12 GPa while it is reduced at 20 GPa due to the renormalizations that quantum ionic fluctuations introduce over the phonon spectra, and the length of the B-H bond. At 12 GPa quantum effects stretch the B-H bond by about 1%. The value of ω_{\log} is about the same at 12 GPa, but by

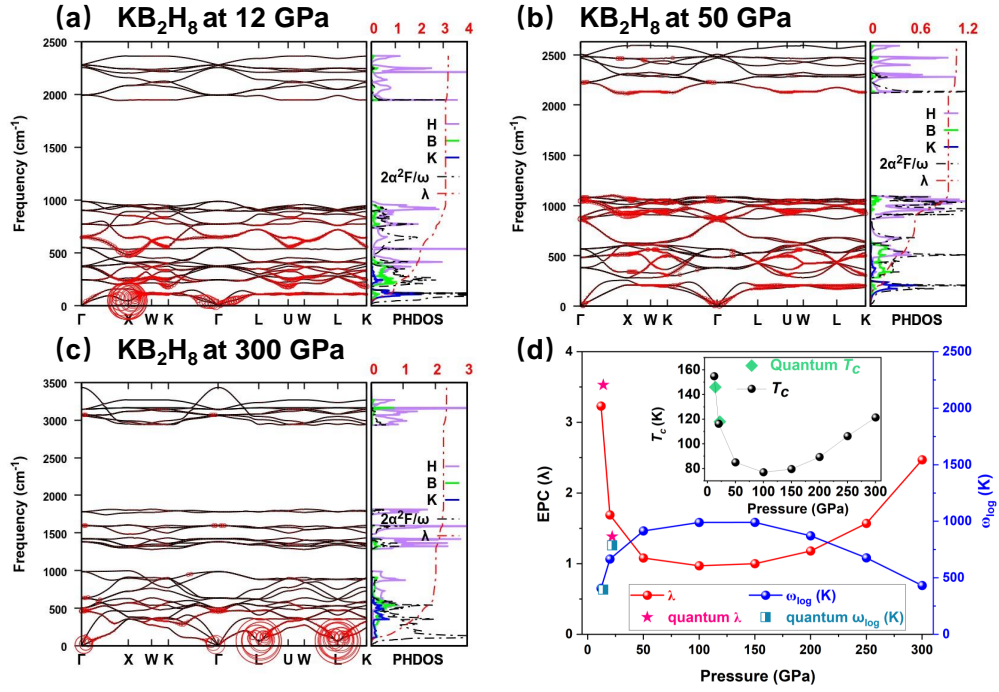


Figure 6: Superconducting properties of KB_2H_8 . Phonon band structures, atom projected phonon density of states (PHDOS), Eliashberg spectral function scaled by the frequency ($2\alpha^2F/\omega$), and the EPC integral ($\lambda(\omega)$) at various pressures: (a) 12 GPa, (b) 50 GPa, and (c) 300 GPa. The radius of the bubble on the phonon dispersion curve is proportional to the electron-phonon coupling constant ($\lambda_{q\nu}$) for the mode ν at wavevector \mathbf{q} . (d) The total λ and ω_{\log} (logarithmic average frequency) as a function of pressure. The resulting T_c , as computed via the Migdal-Eliashberg formalism with $\mu^* = 0.1$, is shown in the inset. Superconducting properties obtained considering quantum fluctuations at 14 and 22 GPa of quantum pressure are also provided.

20 GPa quantum nuclear effects decrease it by $\sim 20\%$. These variations are related to the sustained soft mode at the X -point and to the increased separation between the lower and central optical branches (Figure S27). Calculating the value of T_c through the Migdal-Eliashberg formalism, we find it to be slightly reduced at 12 GPa, where the variation over the phonon spectra are more significant while at 20 GPa it remains almost identical to the classical case.

Recently, a LaBeH₈ phase has been synthesized under pressure with a T_c rivaling some of the cuprates (110 K at 80 GPa) [30]. The KB₂H₈ phase studied here is predicted to be stable to even lower pressures and exhibit an even higher T_c . We therefore wondered if it could be made? Though dynamic stability is easy to assess, it is not the only important criteria for predicting the feasibility of new materials with superlative properties. Thermodynamic stability often necessitates laborious CSP searches that may, or may not, identify the thermodynamic minimum, and cannot pinpoint phases that are metastable and synthesizable. Another type of stability that is easier to probe computationally is kinetic or thermal stability as estimated via molecular dynamics (MD) simulations. Our computations showed that at 12 GPa KB₂H₈ decomposes even at 77 K (Figure 7); further analysis of the structure present at the end of the simulation revealed BH₄⁻ molecules, along with species that could be characterized as BH₃ units to which H₂^{δ-} was bonded side-on and (H₃B-H-BH₃)⁻ fragments. Unsurprisingly, this decomposed phase is a PBE-semimetal. The plot of the energy evolution as a function of time of an MD run performed at 77 K illustrates a steep decrease of energy within the first picosecond, indicative of a structural transformation. At 50 GPa, however, pressure coerced the $Fm\bar{3}m$ KB₂H₈ structure to persist up to at least 165 K, suggesting this phase, should it be made, would not fall apart below its superconducting critical temperature. Notably, while LaBeH₈ has a superconducting figure [82] of merit, S , of 1.236 at 80 GPa, $S = 1.340$ for KB₂H₈ at 50 GPa.

4. Conclusion

This manuscript presents a survey of MX_2H_8 ($M = \text{Li, Na, K, Rb, Cs, Be, Mg, Ca, Sr, Ba, Sc, Y, and La, } X = \text{B or C}$) phases derived from the clathrate-like MH_{10} superhydrides, featuring either CH₄ or BH₄⁻ molecular-like subunits. Fourteen of these, six of which had not been reported before, were identified as dynamically stable at some pressure between 0-300 GPa. A DFT-Chemical pressure analysis showed that the size of the M atom could play a significant role in the dynamical stability of the MB_2H_8 ($M = \text{alkali}$) family. In all cases, the elec-

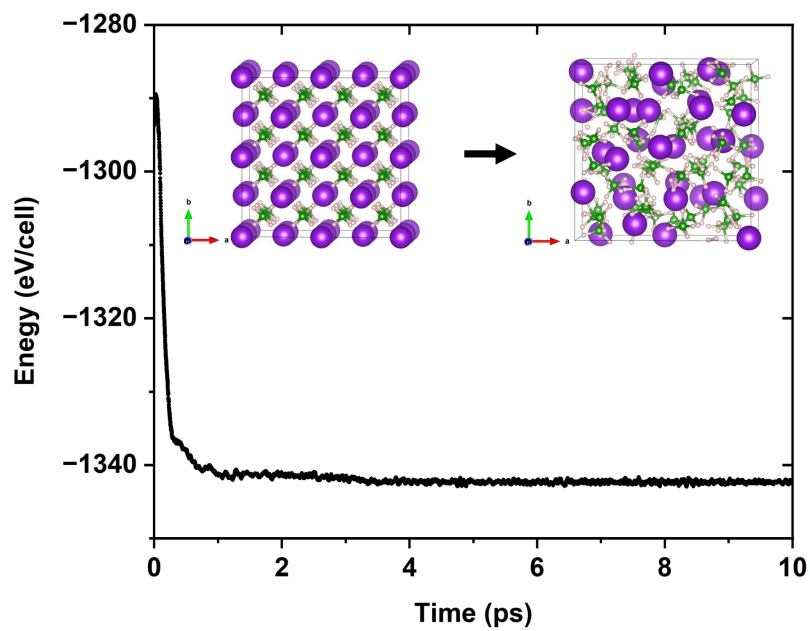


Figure 7: Plot of energy versus simulation time in a first-principles molecular dynamics simulation on a supercell of KB_2H_8 at 77 K and 12 GPa. During the first picosecond of the simulation the structure overcomes a barrier and transitions to a phase containing K^+ and various molecular B-H containing units, as shown in the inset. K/B/H atoms are purple/green/pink.

tropositive metal atoms donate electrons to the CH_4 and BH_4^- subunits, with the metal valency dictating the placement of the Fermi level and the number of occupied states. Generally, univalent or trivalent metals produce the highest density of states at the Fermi level, positioning them as the strongest candidates for superconductivity, while bivalent metals lead to insulators or semimetals. However, MC_2H_8 phases with univalent M atoms display electrone-like behavior due to the overlap of diffuse orbitals, which are unoccupied within neutral methane, that become occupied upon donation of electron density from M , generally suppressing their superconducting behavior due to the poor EPC associated with electrone-like phases. The highest T_c s are predicted to occur for the alkali-metal MB_2H_8 phases, with a pressure dependence showing higher T_c s at the extrema of the pressure range studied and decreasing at intermediate pressures. The strongest contributions to the EPC of these systems involved rocking and twisting motions of the BH_4^- units. Computations on KB_2H_8 taking quantum nuclear effects into account stabilize low-frequency phonons at low pressures, bringing the onset of dynamical instability to 5, rather than 12 GPa, albeit with a slight decrease in estimated T_c at 12 GPa.

Although these results show great promise for KB_2H_8 as a warm and light superconductor, *ab initio* molecular dynamics simulations reveal a crucial issue for potential synthetic attempts – KB_2H_8 undergoes decomposition above 77 K at 12 GPa, and can only be stabilized up to 165 K with compression to 50 GPa. Nonetheless, the superconducting figure of merit predicted for KB_2H_8 rivals that of a recently synthesized LaBeH_8 phase [30]. These results highlight that kinetic and thermal effects are of key importance in the prediction of viable superconductors. A vast phase-space remains to be explored to find a superconducting phase under ambient conditions, whether prompted by modification of high-pressure phases or with altogether new geometries identified by crystal structure prediction or machine learning efforts.

Supporting Information

Supplementary data to this article can be found online at It includes the computational details, electronic band structures and densities of states, thermodynamic and thermal (molecular dynamics) stability analysis, Bader charges, structural parameters, Eliashberg spectral functions, phonon dispersion curves, EPC calculations, and details of the chemical pressure calculations.

Acknowledgments

We acknowledge the U.S. National Science Foundation for financial support, specifically grants DMR-2132491 (N.G.) and DMR-2136038 (F.B.). K.H. is thankful to the U.S. Department of Energy, National Nuclear Security Administration, through the Capital-DOE Alliance Center under Cooperative Agreement DE-NA0003975 for financial support. Calculations were performed at the Center for Computational Research at SUNY Buffalo [83].

References

- [1] L. Boeri, R. Hennig, P. Hirschfeld, G. Profeta, A. Sanna, E. Zurek, W. E. Pickett, M. Amsler, R. Dias, M. I. Eremets, et al., The 2021 room-temperature superconductivity roadmap, *J. Phys.: Condens. Matter* 34 (2022) 183002.
- [2] N. W. Ashcroft, Hydrogen dominant metallic alloys: High temperature superconductors?, *Phys. Rev. Lett.* 92 (2004) 187002.
- [3] A. P. Drozdov, M. I. Eremets, I. A. Troyan, V. Ksenofontov, S. I. Shylin, Conventional superconductivity at 203 Kelvin at high pressures in the sulfur hydride system, *Nature* 525 (2015) 73–76.
- [4] M. Somayazulu, M. Ahart, A. K. Mishra, Z. M. Geballe, M. Baldini, Y. Meng, V. V. Struzhkin, R. J. Hemley, Evidence for superconductivity above 260 K in lanthanum superhydride at megabar pressures, *Phys. Rev. Lett.* 122 (2019) 027001.
- [5] A. P. Drozdov, P. P. Kong, V. S. Minkov, S. P. Besedin, M. A. Kuzovnikov, S. Mozaffari, L. Balicas, F. F. Balakirev, D. E. Graf, V. B. Prakapenka, et al., Superconductivity at 250 K in lanthanum hydride under high pressures, *Nature* 569 (2019) 528–531.
- [6] P. Kong, V. S. Minkov, M. A. Kuzovnikov, A. P. Drozdov, S. P. Besedin, S. Mozaffari, L. Balicas, F. F. Balakirev, V. B. Prakapenka, S. Chariton, et al., Superconductivity up to 243 K in the yttrium–hydrogen system under high pressure, *Nat. Commun.* 12 (2021) 5075.

- [7] I. A. Troyan, D. V. Semenov, A. G. Kvashnin, A. V. Sadakov, O. A. Sobolevskiy, V. M. Pudalov, A. G. Ivanova, V. B. Prakapenka, E. Greenberg, A. G. Gavriluk, et al., Anomalous high-temperature superconductivity in YH_6 , *Adv. Mater.* 33 (2021) 2006832.
- [8] L. Ma, K. Wang, Y. Xie, X. Yang, Y. Wang, M. Zhou, H. Liu, X. Yu, Y. Zhao, H. Wang, et al., High-temperature superconducting phase in clathrate calcium hydride CaH_6 up to 215 K at a pressure of 172 GPa, *Phys. Rev. Lett.* 128 (2022) 167001.
- [9] Z. Li, X. He, C. Zhang, X. Wang, S. Zhang, Y. Jia, S. Feng, K. Lu, J. Zhao, J. Zhang, et al., Superconductivity above 200 K discovered in superhydrides of calcium, *Nat. Commun.* 13 (2022) 2863.
- [10] D. V. Semenov, I. A. Troyan, A. G. Ivanova, A. G. Kvashnin, I. A. Kruglov, M. Hanfland, A. V. Sadakov, O. A. Sobolevskiy, K. S. Pervakov, I. S. Lyubutin, et al., Superconductivity at 253 K in lanthanum-yttrium ternary hydrides, *Mater. Today* 48 (2021) 18–28.
- [11] K. P. Hilleke, E. Zurek, Tuning chemical precompression: Theoretical design and crystal chemistry of novel hydrides in the quest for warm and light superconductivity at ambient pressures, *J. Appl. Phys.* 131 (2022) 070901.
- [12] E. Zurek, T. Bi, High-temperature superconductivity in alkaline and rare earth polyhydrides at high pressure: A theoretical perspective, *J. Chem. Phys.* 150 (2019) 050901.
- [13] J. A. Flores-Livas, L. Boeri, A. Sanna, G. Profeta, R. Arita, M. Eremets, A perspective on conventional high-temperature superconductors at high pressure: Methods and materials, *Phys. Rep.* 856 (2020) 1–78.
- [14] H. Wang, J. S. Tse, K. Tanaka, T. Iitaka, Y. Ma, Superconductive sodalite-like clathrate calcium hydride at high pressures, *Proc. Natl. Acad. Sci. U.S.A.* 109 (2012) 6463–6466.
- [15] H. Liu, I. I. Naumov, R. Hoffmann, N. Ashcroft, R. J. Hemley, Potential high- T_c superconducting lanthanum and yttrium hydrides at high pressure, *Natl. Acad. Sci. U. S. A.* 114 (2017) 6990–6995.

- [16] F. Peng, Y. Sun, C. J. Pickard, R. J. Needs, Q. Wu, Y. Ma, Hydrogen clathrate structures in rare earth hydrides at high pressures: Possible route to room-temperature superconductivity, *Phys. Rev. Lett.* 119 (2017) 107001.
- [17] D. Duan, Y. Liu, F. Tian, D. Li, X. Huang, Z. Zhao, H. Yu, B. Liu, W. Tian, T. Cui, Pressure-induced metallization of dense $(\text{H}_2\text{S})_2\text{H}_2$ with high- T_c superconductivity, *Sci. Rep.* 4 (2014) 6968.
- [18] T. Bi, N. Zarifi, T. Terpstra, E. Zurek, The search for superconductivity in high pressure hydrides, in: J. Reedijk (Ed.), *Reference Module in Chemistry, Molecular Sciences and Chemical Engineering*, Elsevier, Waltham, MA, 2019, pp. 1–36.
- [19] P. T. Salzbrenner, S. H. Joo, L. J. Conway, P. I. C. Cooke, B. Zhu, M. P. Matraszek, W. C. Witt, C. J. Pickard, Developments and further applications of ephemeral data derived potentials, *J. Chem. Phys.* 159 (2023) 144801.
- [20] P. P. Ferreira, L. J. Conway, A. Cucciari, S. Di Cataldo, F. Giannessi, E. Kogler, L. T. F. Eleno, C. J. Pickard, C. Heil, L. Boeri, Search for ambient superconductivity in the Lu-N-H system, *Nat. Commun.* 14 (2023) 5367.
- [21] K. Dolui, L. J. Conway, C. Heil, T. A. Strobel, R. Prasankumar, C. J. Pickard, Feasible route to high-temperature ambient-pressure hydride superconductivity, *arXiv preprint* (2023) arXiv:2310.07562.
- [22] Y. Yan, T. Bi, N. Geng, X. Wang, E. Zurek, A metastable CaSH_3 phase composed of HS honeycomb sheets that is superconducting under pressure, *J. Phys. Chem. Lett.* 11 (2020) 9629–9636.
- [23] N. Geng, T. Bi, E. Zurek, Structural diversity and superconductivity in S–P–H ternary hydrides under pressure, *J. Phys. Chem. C* 126 (2022) 7208–7220.
- [24] Y. Ge, F. Zhang, R. P. Dias, R. J. Hemley, Y. Yao, Hole-doped room-temperature superconductivity in $\text{H}_3\text{S}_{1-x}\text{Z}_x$ ($\text{Z}=\text{C}, \text{Si}$), *Mater. Today Phys.* 15 (2020) 100330.
- [25] X. Wei, X. Hao, A. Bergara, E. Zurek, X. Liang, L. Wang, X. Song, P. Li, L. Wang, G. Gao, et al., Designing ternary superconducting hydrides with A15-type structure at moderate pressures, *Mater. Today Phys.* 34 (2023) 101086.

- [26] R. Lucrezi, S. Di Cataldo, W. von der Linden, L. Boeri, C. Heil, In-silico synthesis of lowest-pressure high- T_c ternary superhydrides, *npj Computational Materials* 8 (2022) 119.
- [27] Z. Zhang, T. Cui, M. J. Hutcheon, A. M. Shipley, H. Song, M. Du, V. Z. Kresin, D. Duan, C. J. Pickard, Y. Yao, Design principles for high temperature superconductors with hydrogen-based alloy backbone at moderate pressure, *Phys. Rev. Lett.* 128 (2022) 047001.
- [28] X. Liang, A. Bergara, X. Wei, X. Song, L. Wang, R. Sun, H. Liu, R. J. Hemley, L. Wang, G. Gao, *et al.*, Prediction of high- T_c superconductivity in ternary lanthanum borohydrides, *Phys. Rev. B.* 104 (2021) 134501.
- [29] S. Di Cataldo, C. Heil, W. von der Linden, L. Boeri, LaBH₈: Towards high- T_c low-pressure superconductivity in ternary superhydrides, *Phys. Rev. B* 104 (2021) L020511.
- [30] Y. Song, J. Bi, Y. Nakamoto, K. Shimizu, H. Liu, B. Zou, G. Liu, H. Wang, Y. Ma, Stoichiometric ternary superhydride LaBeH₈ as a new template for high-temperature superconductivity at 110 K under 80 GPa, *Physical Review Letters* 130 (2023) 266001.
- [31] M.-J. Jiang, Y.-L. Hai, H.-L. Tian, H.-B. Ding, Y.-J. Feng, C.-L. Yang, X.-J. Chen, G.-H. Zhong, High-temperature superconductivity below 100 GPa in ternary C-based hydride MC₂H₈ with molecular crystal characteristics (M= Na, K, Mg, Al, and Ga), *Phys. Rev. B* 105 (2022) 104511.
- [32] K. Hilleke, E. Zurek, Rational design of superconducting metal hydrides via chemical pressure tuning, *Angew. Chem. Int. Ed.* 61 (2022) e202207589.
- [33] A. P. Durajski, R. Szczyński, New superconducting superhydride LaC₂H₈ at relatively low stabilization pressure, *Phys. Chem. Chem. Phys.* 23 (2021) 25070–25074.
- [34] S. Li, H. Wang, W. Sun, C. Lu, F. Peng, Superconductivity in compressed ternary alkaline boron hydrides, *Phys. Rev. B* 105 (2022) 224107.
- [35] M. Gao, X.-W. Yan, Z.-Y. Lu, T. Xiang, Phonon-mediated high-temperature superconductivity in the ternary borohydride KB₂H₈ under pressure near 12 GPa, *Phys. Rev. B* 104 (2021) L100504.

- [36] Z. Wan, R. Zhang, Metallization of hydrogen by intercalating ammonium ions in metal fcc lattices at lower pressure, *Appl. Phys. Lett.* 121 (2022) 192601.
- [37] N. Geng, K. P. Hilleke, L. Zhu, X. Wang, T. A. Strobel, E. Zurek, Conventional high-temperature superconductivity in metallic, covalently bonded, binary-guest C–B clathrates, *J. Am. Chem. Soc.* 145 (2023) 1696–1706.
- [38] G. Kresse, J. Hafner, *Ab initio* molecular dynamics for liquid metals, *Phys. Rev. B.* 47 (1993) 558–561.
- [39] G. Kresse, D. Joubert, From ultrasoft pseudopotentials to the projector augmented-wave method, *Phys. Rev. B.* 59 (1999) 1758–1775.
- [40] J. P. Perdew, K. Burke, M. Ernzerhof, Generalized gradient approximation made simple, *Phys. Rev. Lett.* 77 (1996) 3865–3868.
- [41] P. E. Blöchl, Projector augmented-wave method, *Phys. Rev. B* 50 (1994) 17953–17979.
- [42] S. Maintz, V. L. Deringer, A. L. Tchougréeff, R. Dronskowski, Lobster: A tool to extract chemical bonding from plane-wave based DFT, *J. Comput. Chem.* 37 (2016) 1030–1035.
- [43] S. Nosé, A unified formulation of the constant temperature molecular dynamics methods, *J. Chem. Phys.* 81 (1984) 511–519.
- [44] N. Shuichi, Constant temperature molecular dynamics methods, *Prog. Theor. Phys. Supp.* 103 (1991) 1–46.
- [45] W. G. Hoover, Canonical dynamics: Equilibrium phase-space distributions, *Phys. Rev. A* 31 (1985) 1695–1697.
- [46] D. Frenkel, B. Smit, *Understanding Molecular Simulation: from Algorithms to Applications*, Elsevier, Amsterdam, Netherlands, 2023.
- [47] A. Togo, I. Tanaka, First principles phonon calculations in materials science, *Scr. Mater.* 108 (2015) 1–5.
- [48] P. Giannozzi, S. Baroni, N. Bonini, M. Calandra, R. Car, C. Cavazzoni, D. Ceresoli, G. L. Chiarotti, M. Cococcioni, I. Dabo, et al., Quantum espresso: A modular and open-source software project for quantum simulations of materials, *J. Phys.: Condens. Matter* 21 (2009) 395502.

- [49] A. Dal Corso, Pseudopotentials periodic table: From H to Pu, *Comput. Mater. Sci.* 95 (2014) 337–350.
- [50] N. Troullier, J. L. Martins, Efficient pseudopotentials for plane-wave calculations, *Phys. Rev. B* 43 (1991) 1993–2006.
- [51] M. Methfessel, A. T. Paxton, High-precision sampling for brillouin-zone integration in metals, *Phys. Rev. B* 40 (1989) 3616–3621.
- [52] P. B. Allen, R. C. Dynes, Transition temperature of strong-coupled superconductors reanalyzed, *Phys. Rev. B* 12 (1975) 905–922.
- [53] G. M. Eliashberg, Interactions between electrons and lattice vibrations in a superconductor, *Sov. Phys. JETP* 11 (1960) 696–702.
- [54] L. Monacelli, R. Bianco, M. Cherubini, M. Calandra, I. Errea, F. Mauri, The stochastic self-consistent harmonic approximation: Calculating vibrational properties of materials with full quantum and anharmonic effects, *J. Phys.: Condens. Matter* 33 (2021) 363001.
- [55] D. C. Fredrickson, DFT-Chemical Pressure analysis: Visualizing the role of atomic size in shaping the structures of inorganic materials, *J. Am. Chem. Soc.* 134 (2012) 5991–5999.
- [56] V. M. Berns, J. Engelkemier, Y. Guo, B. J. Kilduff, D. C. Fredrickson, Progress in visualizing atomic size effects with DFT-chemical pressure analysis: From isolated atoms to trends in AB_5 intermetallics, *J. Chem. Theory Comput.* 10 (2014) 3380–3392.
- [57] K. P. Hilleke, D. C. Fredrickson, Discerning chemical pressure amidst weak potentials: Vibrational modes and dumbbell/atom substitution in intermetallic aluminides, *J. Phys. Chem. A* 122 (2018) 8412–8426.
- [58] E. Lu, J. Van Buskirk, J. Cheng, D. C. Fredrickson, Tutorial on chemical pressure analysis: How atomic packing drives laves/zintl intergrowth in K_3Au_5Ti , *Crystals* 11 (2021) 906.
- [59] X. Gonze, B. Amadon, G. Antonius, F. Arnardi, L. Baguet, J.-M. Beuken, J. Bieder, F. Bottin, J. Bouchet, E. Bousquet, Brouwer, et al., The Abinit project: Impact, environment and recent developments, *Comput. Phys. Commun.* 248 (2020) 107042.

- [60] A. P. Durajski, R. Szczyński, First-principles estimation of low-pressure superconductivity in KC_2H_8 ternary hydride, *Phys. Status Solidi Rapid Res. Lett.* (2023).
- [61] V. M. Berns, D. C. Fredrickson, Structural plasticity: How intermetallics deform themselves in response to chemical pressure, and the complex structures that result, *Inorg. Chem.* 53 (2014) 10762–10771.
- [62] A. Lim, D. C. Fredrickson, Entropic control of bonding, guided by chemical pressure: Phase transitions and 18-n+m isomerism of IrIn_3 , *Inorg. Chem.* 62 (2023) 10833–10846.
- [63] A. M. Shipley, M. J. Hutcheon, R. J. Needs, C. J. Pickard, High-throughput discovery of high-temperature conventional superconductors, *Phys. Rev. B* 104 (2021) 054501.
- [64] M.-J. Jiang, H.-L. Tian, Y.-L. Hai, N. Lu, P.-F. Tong, S.-Y. Wu, W.-J. Li, C.-L. Yang, G.-H. Zhong, Phonon-mediated low-pressure superconductivity in ternary hydride Ba-CH_4 , *ACS Appl. Electron. Mater.* 3 (2021) 4172–4179.
- [65] H.-Y. Lv, S.-Y. Zhang, M.-H. Li, Y.-L. Hai, N. Lu, W.-J. Li, G.-H. Zhong, Metallization and superconductivity in methane doped by beryllium at low pressure, *Phys. Chem. Chem. Phys.* 22 (2020) 1069–1077.
- [66] F. Tian, D. Duan, X. Sha, Y. Liu, T. Yang, B. Liu, T. Cui, Predicted structures and superconductivity of hypothetical Mg-CH_4 compounds under high pressures, *Mater. Res. Express* 2 (2015) 046001.
- [67] S. Di Cataldo, L. Boeri, Metal borohydrides as ambient-pressure high- T_c superconductors, *Phys. Rev. B* 107 (2023) L060501.
- [68] C. Kokail, W. von der Linden, L. Boeri, Prediction of high- T_c conventional superconductivity in the ternary lithium borohydride system, *Phys. Rev. Mater.* 1 (2017) 074803.
- [69] M. Gao, P.-J. Guo, H.-C. Yang, Y. X.-W., M. F., Z.-Y. Lu, T. Xiang, H.-Q. Lin, Stabilizing a hydrogen rich superconductor at 1 GPa by charge transfer modulated virtual high-pressure effect, *Phys. Rev. B* 107 (2023) L180501.
- [70] S. Di Cataldo, W. von der Linden, L. Boeri, Phase diagram and superconductivity of calcium borohydrides at extreme pressures, *Phys. Rev. B* 102 (2020) 014516.

- [71] X. Li, X. Zhang, A. Bergara, Y. Liu, G. Yang, Structural and electronic properties of Na-B-H compounds at high pressure, *Phys. Rev. B* 106 (2022) 174104.
- [72] E. Zurek, P. P. Edwards, R. Hoffmann, A molecular perspective on lithium-ammonia solutions, *Angew. Chem. Int. Ed.* 48 (2009) 8198–8232.
- [73] E. Zurek, X.-D. Wen, R. Hoffmann, (Barely) Solid $\text{Li}(\text{NH}_3)_4$: The electronics of an expanded metal, *J. Am. Chem. Soc.* 133 (2011) 3535–3547.
- [74] Y. Sun, M. Miao, Chemical templates that assemble the metal superhydrides, *Chem* 9 (2023) 443–459.
- [75] R. S. Kumar, E. Kim, A. L. Cornelius, Structural phase transitions in the potential hydrogen storage compound KBH_4 under compression, *J. Phys. Chem. C* 112 (2008) 8452–8457.
- [76] C. Heil, S. di Cataldo, G. B. Bachelet, L. Boeri, Superconductivity in sodalite-like yttrium hydride clathrates, *Phys. Rev. B* 99 (2019) 220502.
- [77] X. Zhang, G. Yang, Recent advances and applications of inorganic electrides, *J. Phys. Chem. Lett.* 11 (2020) 3841–3852.
- [78] F. Belli, T. Novoa, J. Contreras-Garcia, I. Errea, Strong correlation between electronic bonding network and critical temperature in hydrogen-based superconductors, *Nat. Commun.* 12 (2021) 5381.
- [79] I. Errea, M. Calandra, C. J. Pickard, J. R. Nelson, R. J. Needs, Y. Li, H. Liu, Y. Zhang, Y. Ma, F. Mauri, Quantum hydrogen-bond symmetrization in the superconducting hydrogen sulfide system, *Nature* 532 (2016) 81–84.
- [80] F. Belli, I. Errea, Impact of ionic quantum fluctuations on the thermodynamic stability and superconductivity of LaBH_8 , *Phys. Rev. B* 106 (2022) 134509.
- [81] I. Errea, F. Belli, L. Monacelli, A. Sanna, T. Koretsune, T. Tadano, R. Bianco, M. Calandra, R. Arita, F. Mauri, et al., Quantum crystal structure in the 250-Kelvin superconducting lanthanum hydride, *Nature* 578 (2020) 66–69.
- [82] C. J. Pickard, I. Errea, M. I. Eremets, Superconducting hydrides under pressure, *Annu. Rev. Condens. Matter Phys.* 11 (2020) 57–76.

[83] Center for Computational Research, University at Buffalo., 2023.
[Http://hdl.handle.net/10477/79221](http://hdl.handle.net/10477/79221) (accessed December 22nd, 2023).